Sensitive quantum tiltmeter with nanoradian resolution

Jie Liu, Wen-Jie Xu, Cheng Zhang, Qin Luo ◉, Zhong-Kun Hu, and Min-Kang Zhou ◉*

MOE Key Laboratory of Fundamental Physical Quantities Measurement, Hubei Key Laboratory of Gravitation and Quantum Physics, PGMF, School of Physics, Huazhong University of Science and Technology, Wuhan 430074, China

Precision tilt measurements are becoming more and more important in fundamental research and crustal deformation observations. A quantum tiltmeter based on atom interferometry could be among the most stable tiltmeters in theory but is currently constrained by the low resolution. Here, we demonstrate an extremely sensitive quantum tiltmeter with the configuration of a Mach-Zehnder-type atom interferometer for precisely measuring the crustal deformation. The scheme of two pairs of Raman beams sharing one retroreflection mirror effectively increases the scale factor, making this quantum tiltmeter achieve a sensitivity of 40 $\text{nrad}/\text{Hz}^{1/2}$ and a resolution of 1.8 nrad within an integration time of 640 s for tilt measurements, which represents an improvement on the sensitivity by a factor of 32 comparing to previous work. The Earth tilt tide lasting for 63 h has been observed with high signal-to-noise ratio by our quantum tiltmeter, which paves the way to study the crustal deformation with a quantum sensor.

I. INTRODUCTION

Developing high-precision quantum sensor and exploring new applications are engaging lots of attention both in modern science and in fundamental research. Atom interferometers (AIs) have been demonstrated to be powerful sensors for high-precision measurements, such as measuring the gravity [1–6], the gravity gradient [7–10], the Newtonian gravitational constant G [11,12], the rotation [13,14], the magnetic-field gradient [15], as well as the test of fundamental physics [16–20]. In recent years, quantum tiltmeters based on atom interferometry have been constructed [21–24]. Since the tilt angle we extracted is referred to the direction of gravity, we can obtain the absolute tilt angle between the Raman beams and the horizontal plane. Moreover, the measurement of the tilt angle is linked to the atomic transition line of ^{87}Rb; it will have a good long-term stability in theory. Based on the advantages of this type of tiltmeter, the sensitive quantum tiltmeters can be employed to observe the crustal deformation, which is of great interest in the Earth tide studies [25,26], volcanology [27,28], seismology [29], and geophysics [30,31]. In addition, the quantum tiltmeters can be used in the tilt angle measurements and corrections of scientific facilities for fundamental research. For example, the quantum tiltmeters can be integrated into quantum sensors, such as atom gyroscopes [13,14,32] and atom gravimeters [3,6,17], to realize the *in situ* measurements of the tilt angle and multiaxis measurements, especially in the large-area atom interferometer gyroscopes, this tiltmeter can be employed for the self-alignment of the separated Raman beams. In the large ring laser gyroscope [33,34] and the advanced Laser Interferometer Gravitational Wave Observatory [35,36], the long-term slow tilt fluctuations

need to be monitored and corrected. Generally speaking, a sensitive and stable quantum tiltmeter will excite common interest in geoscience and in atomic, molecular, and optical physics. However, the sensitivities and resolutions of current quantum tiltmeters (10^{-6}-$\text{rad}/\text{Hz}^{1/2}$ level) cannot meet the requirements of these applications, and it is lower than the traditional tiltmeters, such as the long-baseline water-tube tiltmeters [37,38], various forms of pendulum tiltmeters [39–42], bubble tiltmeters [43], and laser tiltmeters [44]. Thus, improving the sensitivity and resolution are the priority in the development of quantum tiltmeters.

In this paper, we report an enhanced quantum tiltmeter with a large-scale ^{87}Rb atom interferometer. This tiltmeter is constructed with two Raman beams sharing one retroreflecting mirror, which promises a substantial improvement for the scale factor. The intersection angle between the two Raman beams is 2.54(7) μrad on the *y-z* plane measured by the interferometer itself, and the fringe contrast is about 28% with an interrogation time of $2T = 299.2$ ms. Then, we analyze the effect of air density inhomogeneity on the tilt measurements in detail and suppress it with a heat insulation cover. The sensitivity of tilt measurements is 40 $\text{nrad}/\text{Hz}^{1/2}$ after the vibration correction and the resolution down to 1.8 nrad within an integration time of 640 s. Finally, a 63-h continuous tilt tide in the east-west direction has been observed clearly, which shows that this quantum tiltmeter has a great capability in monitoring the crustal deformation.

II. PRINCIPLE AND SCHEME

A. Principle

The principle of the quantum tiltmeter is illustrated in Fig. 1(a). We utilize the MZ-type interferometer based on two-photon-stimulated Raman transitions with a $\pi/2 - \pi - \pi/2$
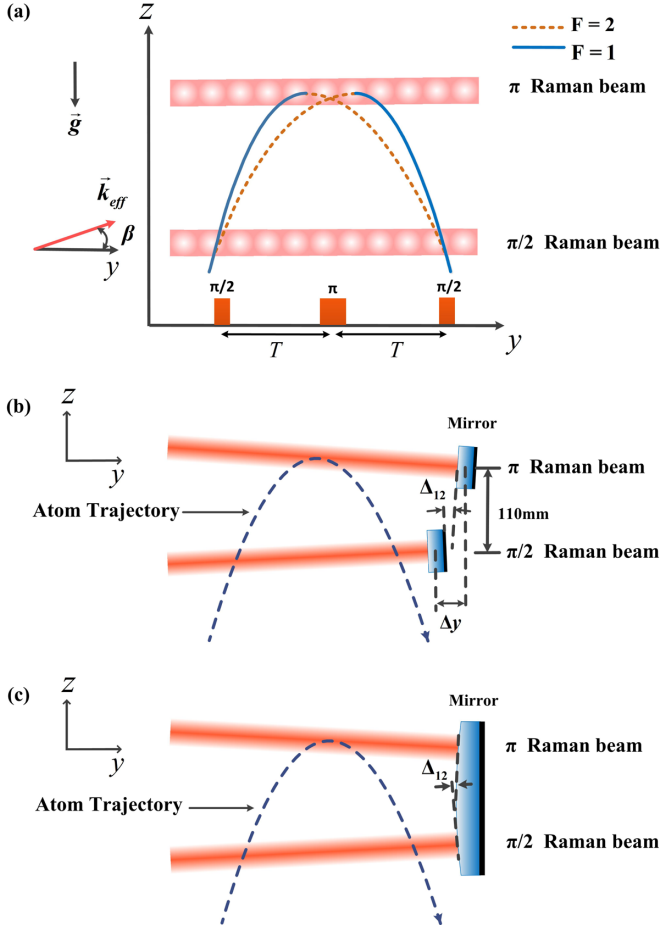
*zmk@hust.edu.cn

FIG. 1. Principle of the quantum tiltmeter. (a) The space-time diagram of the Mach-Zehnder (MZ)-type interferometer. (b) Schematic of the Raman beams' configuration. Two pairs of Raman beams with two reflecting mirrors, and the vertical distance is 110 mm. The intersection angle of two Raman beams on the y-z plane is Δ_{12}, and Δy is the displacement difference of two Raman mirrors in the y-axis direction. (c) Two pairs of Raman beams sharing one large-scale reflecting mirror.

Raman pulses sequence to coherently split, reflect, and finally combine the atomic wave packet [1,45]. After the sequence, the mean transition probability P of the atoms can be determined as $P = (1 - C \cos \Delta \phi)/2$, where C is the contrast of the interferometry fringe and $\Delta \phi$ is the total phase shift of the atom interferometer. In a uniform gravity field, the phase shift $\Delta \phi$ is given by

$$\Delta \phi = (\vec{k}_{\text{eff}} \cdot \vec{g} - \alpha)T^2, \tag{1}$$

where $\vec{k}_{\text{eff}}$ is the effective wave vector of the Raman lasers, $\vec{g}$ is the local gravitational acceleration, T is the separation time between two adjacent Raman pulses, and α is the frequency chirp rate of the Raman beams. In our experiment, the Raman beams propagate in the quasihorizontal direction, and the angle between the wave-vector $\vec{k}_{\text{eff}}$ and the horizontal plane is β, which is the tilt signal that needs to be measured. The formula $\vec{k}_{\text{eff}} \cdot \vec{g}T^2$ can be written as $k_{\text{eff}} gT^2 \sin \beta$, which shows that the tilt angle is extracted by measuring the projection of the gravity in the direction of the Raman beams. As the Raman beams

are tilted in a tiny range (tens of microradians), considering the first-order approximation, Eq. (1) can be simplified as $\Delta \phi = (k_{\text{eff}} g\beta - \alpha)T^2$. When the atom interferometer works at the central fringe, the tilt signal can be written as

$$\beta = \alpha/(k_{\text{eff}} g). \tag{2}$$

Theoretically, the frequency chirp rate α, the wave-vector k_{eff}, and the gravity g can be determined accurately, thus, the absolute tilt angle β can be measured precisely.

B. Configuration scheme of the Raman beams

According to Eq. (1), the scale factor of the tiltmeter is proportional to T^2, and a large-scale quantum tiltmeter needs two Raman beams to increase the interrogation time. The vertical distance of two Raman beams is about 110 mm when the time of two adjacent Raman pulses is 150 ms. As shown in Fig. 1(b), supposing that we adopt two retroreflection mirrors to obtain two counterpropagating Raman beams, respectively, the displacement difference Δy of two Raman mirrors in the y-axis direction will introduce an extra phase $\phi_y = 2k_{\text{eff}} \Delta y$. The tiltmeter with a resolution of 10^{-8} rad requires that the fluctuation of Δy should be smaller than 1 nm. Moreover, Δy is in the state of dynamic change because of the difference of temperature and temperature gradient between the two separated Raman mirrors with two mounts. To decrease the long-term instability caused by Δy, one large-scale rectangular reflecting mirror is used here instead of two independent mirrors [shown in Fig. 1(c)]. For a single mirror with one mount, the effects of temperature are greatly suppressed.

For MZ-type interferometers, the separated two Raman beams should be precisely aligned for combining two interferometric paths to construct a closed interferometric loop [14,32,46]. In other words, the nonparallelism of two Raman beams has a large influence on the fringe contrast. However, as shown in Fig. 1(c), the alignments of two Raman beams cannot be adjusted arbitrarily since only one reflecting mirror is applied here. The intersection angles of two Raman beams are determined by the surface quality of the reflecting mirror, the window of the vacuum chamber, and the $\lambda/4$ wave plate. Considering the y-z plane here, the fringe contrast can be written as [32,46]

$$C = A_{\text{QT}} \exp \left[-\frac{(2k_{\text{eff}} \sigma_{v_z} T \Delta_{12})^2}{2} \right] \exp \left[-\frac{(2k_{\text{eff}} \sigma_z \Delta_{12})^2}{2} \right], \tag{3}$$

where A_{QT} is the maximum contrast of the quantum tiltmeter, Δ_{12} is the intersection angle of two Raman beams on the y-z plane, σ_z and σ_{v_z} are the standard deviations of normal distributions of atomic cloud for initial position and velocity in the z-axis direction, respectively. By substituting the typical parameters in our experiment ($\sigma_z = 2.4$ mm, $\sigma_{v_z} = 3.8$ mm/s, and $T = 150$ ms), it can be theoretically calculated that the value of Δ_{12} corresponding to the full width at half maximum of the contrast is 14.8 μrad. Thus, we need to improve the surface quality of the reflecting mirror to reduce the intersection angles of two Raman beams. In the experiment, we measure the intersection angle between the two Raman beams on the
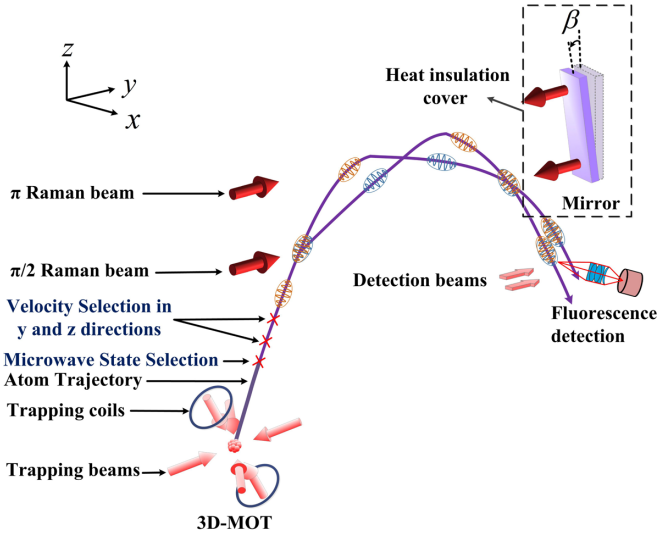
FIG. 2. Experimental setup of the quantum tiltmeter. A heat insulation cover is fixed between the quartz window and the retrore-flection mirror. The tilt angle between the Raman mirror and the plumb line is β, which is the tilt signal that needs to be measured.

y-z plane with the AI tiltmeter itself, the method and result are described in Sec. A of Sec. IV.

III. EXPERIMENTAL SETUP

This quantum tiltmeter is based on an atom interferometer, which is realized in a ultra-high-vacuum chamber, and the structure of the atom interferometer is shown in Fig. 2. About 10^9 ^{87}Rb atoms are trapped by the three-dimensional magneto-optical trap (3D-MOT) within 433 ms. Then, the atomic cloud is launched along a parabolic trajectory with an initial velocity of 4.27 m/s at the angle of 69.3° with respect to the horizontal plane. The temperature of atomic cloud is 2.5 μK after the moving molasses.

In the state-preparation stage, the repumping beam of the 3D-MOT is turned off with a time delay of 10 ms after the moving molasses stage to keep ^{87}Rb atoms in the $|5^2S_{1/2}, F = 2\rangle$ state. Then, the microwave pulse is switched on to stimulate the cold atoms in the magnetic-insensitive hyperfine state $|5^2S_{1/2}, F = 1, m_F = 0\rangle$. After that, a narrow velocity distribution of atoms is obtained through two π-Raman pulses with a Doppler-sensitive configuration [47] in the y and z directions successively. Finally, about 1.2×10^4 cold atoms in state $|5^2S_{1/2}, F = 1, m_F = 0\rangle$ are prepared.

In the interference zone, the Raman beams are composed of two phased-locked lasers [3] with a total power of 90 mW, and the $1/e^2$ diameters are about 26 mm. The $\pi/2$ and π-Raman beams are reflected by a single large-size retroreflection mirror to realize the counterpropagating configuration. The size of the rectangular reflecting mirror is $50 \times 30 \times 150$ mm^3 ($L \times W \times H$). The peak-to-valley and rms value of the reflecting mirror surface quality are 183.5 and 30.9 nm, respectively. The reflecting mirror is fixed on the marble platform ($0.5 \times 0.4 \times 1.51$ m^3) which is firmly connected with the ground. A temperature sensor is placed on the marble platform to monitor the room temperature. In
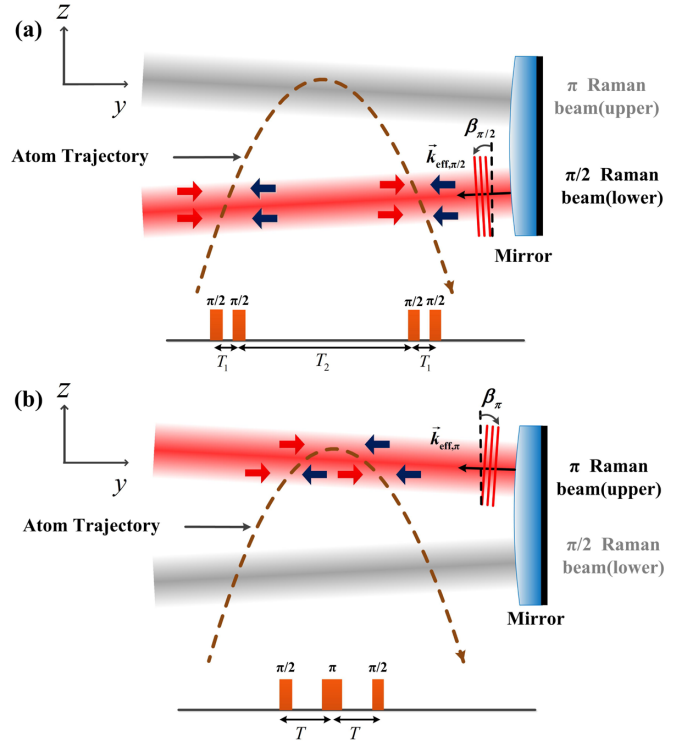

FIG. 3. Schematic of the AI tiltmeter realized by each Raman beam, respectively. (a) The RB-type interferometer is constructed by four $\pi/2$ pulses, which is realized by the lower Raman beam. $\beta_{\pi/2}$ represents the tilt angle between the effective wave vector of the $\pi/2$ Raman beam and the horizontal plane. (b) The MZ-type interferometer is constructed by a sequence of $\pi/2 - \pi - \pi/2$ pulses, which is realized by the upper Raman beam. β_{π} is the tilt angle between the effective wave vector of the-π-Raman beam and the horizontal plane.

addition, a seismometer (CMG-3SEP) next to the mirror is employed to monitor and correct the vibration noise during the experiment [48,49]. The whole interrogation time is restricted by the parabolic trajectory of the atoms and the size of vacuum chamber window. Considering the Raman transition efficiency and the contrast of fringe, the interrogation time is $2T = 299.2$ ms. After the Raman pulses sequence, the transition probability P and fringes are obtained through a normalized fluorescence detection method. Besides, we reverse the wave vectors [2] to reduce some systematic effects, such as the ac-Stark effect and the Zeeman effect [50]. Finally, the phase shift can be extracted from the fringes, and the overall time for one measurement is 1.25 s.

IV. EXPERIMENTAL RESULTS

A. Measuring the intersection angle between the two Raman beams on the y-z plane

To obtain the intersection angle of two Raman beams on the y-z plane, we use each Raman beam to realize a AI tiltmeter, respectively [21]. To make it easier to understand, the π-Raman beam is called upper Raman beam, the $(\pi/2)$-Raman beam is called lower Raman beam. Specifically, as shown in Fig. 3(a), we utilize the lower Raman beam to

build a Ramsey-Bordé- (RB-) type interferometer which is constructed by a sequence of $\pi/2 - \pi/2 - \pi/2 - \pi/2$ pulses where all four $\pi/2$ pulses are realized by the lower Raman beam. In a uniform gravity field, the phase-shift ϕ_{RB} of the RB-type interferometer can be written as

$$\phi_{RB} = (k_{\text{eff},\pi/2} g \beta_{\pi/2} - \alpha_{RB}) T_1 (T_1 + T_2), \tag{4}$$

where $k_{\text{eff},\pi/2}$ is the effective wave vector of the lower Raman beam, g is the local gravitational acceleration, T_1 is the separation time between the first two pulses as well as the last two pulses, T_2 is the separation time between the second and third Raman pulses, and α_{RB} is the frequency chirp rate of the Raman beam. We change the separated time T_1 and keep $T_1 + T_2$ as a constant to find the central fringes, and the tilt angle $\beta_{\pi/2}$ between the $\vec{k}_{\text{eff},\pi/2}$ and the horizontal plane can be determined as

$$\beta_{\pi/2} = \alpha_{RB}/(k_{\text{eff},\pi/2} g). \tag{5}$$

Similarly, for the π-Raman beam as shown in Fig. 3(b), we use the upper Raman beam to build a MZ-type interferometer which is constructed by a sequence of $\pi/2 - \pi - \pi/2$ pulses, where the $\pi/2$ and π pulses are realized by the upper Raman beam. According to Eq. (2), the tilt angle β_π between the $\vec{k}_{\text{eff},\pi}$ and the horizontal plane can be written as

$$\beta_\pi = \alpha_{MZ}/(k_{\text{eff},\pi} g), \tag{6}$$

where $k_{\text{eff},\pi}$ is the effective wave vector of the upper Raman beam, and α_{MZ} is the frequency chirp rate of the Raman beam when the atom interferometer works at the central fringe.

A continuous $\beta_{\pi/2}$ measurement and β_π measurement are carried out for 1800 s, and the average is the value of tilt angle $\beta_{\pi/2}$ and β_π, respectively. Besides, the $\beta_{\pi/2}$ measurements and β_π measurements are repeated three times alternately to confirm the stability of the AI tiltmeter. Finally, the results are shown as blue and red points in Fig. 4, and each data point represents an average of 1800 s. The mean value of tilt angle $\beta_{\pi/2}$ is 19.48(3) μrad, and the mean value of tilt angle β_π is 22.02(6) μrad. Thus, the intersection angle between the two Raman beams is β_π-$\beta_{\pi/2}$ = 2.54(7) μrad on the y-z plane, only corresponding to a lose rate of 2% for the fringe contrast referring to Eq. (3).

B. Interference fringe

As shown in Fig. 5(a), we obtain the interference fringe of the AI tiltmeter with a pulse separation time of 149.6 ms, one fringe comprises ten continuous shots in 12.5 s, and the fringe contrast is about 28%. However, the phase noise is terrible, the mean value of phase uncertainty fitted by the fringes is about 181 mrad, and the sensitivity of tilt measurements is only 520 nrad/Hz$^{1/2}$ (shown as blue line in Fig. 7). To suppress the phase noise and improve the sensitivity of the tiltmeter, the effect of air density inhomogeneity is analyzed in detail as follows:

C. The effect of air density inhomogeneity

In the interference region, the Raman beams propagate through the vacuum chamber and the air to the retroreflection mirror. The length of air passed through by the Raman beams is about 1.5 m. The extra laser phase ϕ_{extra} caused by the air
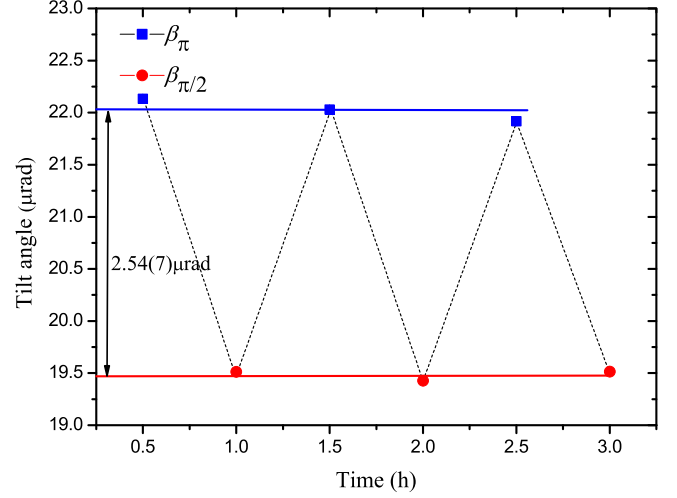

FIG. 4. The results of β_π measurements and $\beta_{\pi/2}$ measurements. Blue square points represent the tilt angle β_π, and the mean value is 22.02(6) μrad (blue line). Red circle points are the tilt angle $\beta_{\pi/2}$, and the mean value is 19.48(3) μrad (red line). The intersection angle of two Raman beams is 2.54(7) μrad on the y-z plane. The $\beta_{\pi/2}$ measurement and β_π measurement are repeated three times alternately, and each data point represents an average of 1800 s

should be considered carefully [32]. The laser phase for the ith Raman pulse $\phi_{\text{air},i}$ introduced by the air refractive index can be expressed as

$$\phi_{\text{air},i} = k_{\text{eff}} l_{\text{air},i} (n_{\text{air},i} - 1), \tag{7}$$

where $n_{\text{air},i}$ represents the refractive index of air at the position of the ith Raman pulse, $l_{\text{air},i}$ is the length of air passed through by the $\pi/2$- or π-Raman beam. The extra laser phase ϕ_{extra} after the interference sequence can be
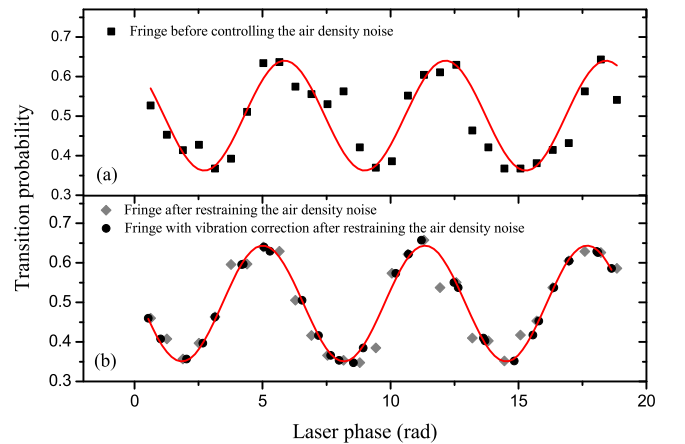

FIG. 5. Fringe pattern of the quantum tiltmeter. (a) The interference fringes before controlling the air density noise. The red solid line is the sinusoidal fit of the ratio of atoms in the $F = 2$ state. (b) The interference fringes after restraining the air density noise with a heat insulation cover. The gray diamond points and black circle points represent the fringes without and with vibration correction, respectively.

written as

$$\phi_{\text{extra}} = \phi_{\text{air},1} - 2\phi_{\text{air},2} + \phi_{\text{air},3}$$
$$= k_{\text{eff}}l_{\text{air},1}(n_{\text{air},1} + n_{\text{air},3} - 2) - 2k_{\text{eff}}l_{\text{air},2}(n_{\text{air},2} - 1).$$
(8)

We consider $l_{\text{air},1}$ is approximately equal to $l_{\text{air},2}$, when the intersection angle between the quartz window and the retroreflection mirror reaches the milliradian level. Besides, in the same position, the refractive indexes of air $n_{\text{air},1}$ and $n_{\text{air},3}$ are approximately invariant within a short interval time (about 0.3 s). Thus, Eq. (8) can be simplified as

$$\phi_{\text{extra}} \approx 2k_{\text{eff}}l_{\text{air}}(n_{\text{air},1} - n_{\text{air},2}) = 2k_{\text{eff}}l_{\text{air}}\Delta n_{\text{air}}, \quad (9)$$

where Δn_{air} represents the difference of air refractive index between the position of $(\pi/2)$- and π-Raman beams. From Eq. (9), the extra Raman laser phase shift derives from the optical path l_{air} and the difference of air refractive indices Δn_{air}.

Different air refractive indices are due to the inhomogeneous air density and distinct temperatures at different positions. Besides, the length of air l_{air} and Δn_{air} will change with the fluctuation of temperature and air density, respectively. To estimate the value of Δn_{air}, two air density sensors (National Institute of Metrology, China, ADMS1306) with the resolution of 1×10^{-4} kg/m^3 are applied to monitor the air density at the position of the $(\pi/2)$- and π-Raman beams respectively. The relationship between the refractive index and the air density can be written as [51,52]

$$(n_{\text{air}} - 1) = \frac{3R'}{2}\rho_{\text{air}}. \quad (10)$$

where ρ_{air} represents the air density and R' called the specific refraction or the refractional invariant. R' can be treated as a constant in our experiment [51,52]. The value of Δn_{air} can be calculated from the different air density by Eq. (10), and the mean value of Δn_{air} is about 1×10^{-7}, which is shown as the black line in Fig. 6. The sampling period of the air density measurement devices is 15 s. Therefore, the extra Raman laser phase noise $\delta\phi_{\text{extra}}$ caused by the variation of Δn_{air} can be calculated by Eq. (7) and gives the limitation of 120 nrad at 15 s for tilt measurements.

To decrease the variation of Δn_{air}, the method in Ref. [32] that fixing a heat insulation cover between the quartz window and the retroreflection mirror (the air pressure inside the cover is still atmospheric) is adopted. The temperature and air density can be evenly distributed in the cylinder cover after a period of stability. Moreover, it can prevent the air convection and reduce the air density fluctuation. With this method help, the mean value of Δn_{air} is decreased to 1×10^{-8} (shown as the red line in Fig. 6), which is about one order of magnitude smaller than before.

D. Sensitivity of the quantum tiltmeter

After restraining the air density noise, the interference fringe of the tiltmeter is shown as gray diamond points in Fig. 5(b). The sensitivity of tilt measurements is displayed by the Allan deviation, and the short-term sensitivity is 103 nrad/Hz$^{1/2}$, which is shown as the magenta line in Fig. 5.
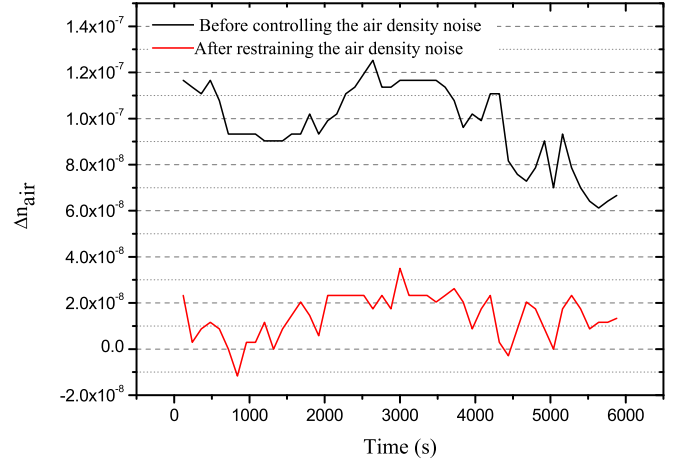

FIG. 6. The difference of air refractive index Δn_{air} between the position of the two Raman beams. The black line represents the value of Δn_{air} before controlling the air density noise, the red line is the value of Δn_{air} after restraining the air density noise by a heat insulation cover.

To suppress the vibration noise, a postcorrection method [48,49] is used here, leading an improvement of the mean value of phase uncertainty from 98 to 28 mrad [shown as black circle points in Fig. 5(b)], corresponding to a resolution of 8 nrad in 12.5 s for tilt measurements. To reach a higher sample rate and higher sensitivity, we adopt the fringe lock technique [49] and use the linear vibration correction to suppress the vibration noise. The sensitivity of tilt measurements is displayed as the red line in Fig. 7, corresponding to a short-term sensitivity of 40 nrad/Hz$^{1/2}$, which represents an
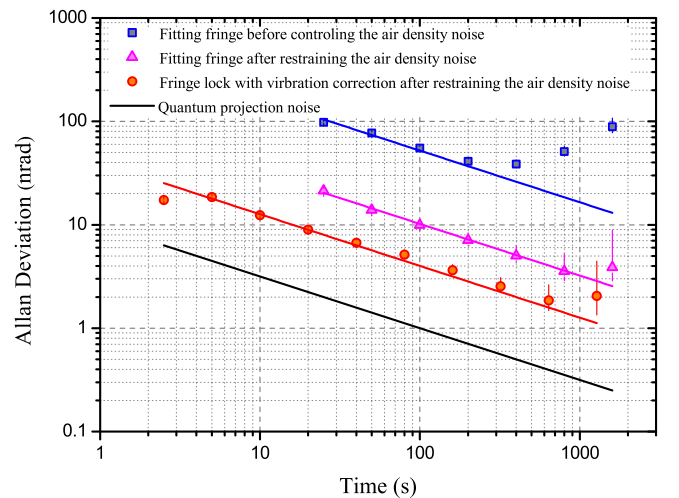

FIG. 7. Allan deviations of the tilt measurements. The blue line gives a short-term sensitivity of 520 nrad/Hz$^{1/2}$ before controlling the air density noise. After restraining the air density noise, the Allan deviation is displayed as the magenta line, corresponding to a sensitivity of 103 nrad/Hz$^{1/2}$. The red line gives a short-term sensitivity of 40 nrad/Hz$^{1/2}$, which represents the Allan deviation by fringe lock with vibration correction after restraining the air density noise. The black line is the limitation of quantum projection noise, corresponding to a noise level of 10 nrad/Hz$^{1/2}$.

improvement of 32 times than previous work in 2017 [21]. The resolution improves as $\tau^{1/2}$ and achieves 1.8 nrad at an integration time of 640 s.

E. Noise tracking

From Eq. (9), the extra Raman laser phase noise $\delta\phi_{\text{extra}}$ is related to the fluctuation of Δn_{air} and l_{air}. For Δn_{air}, since limited by the resolution of the air density sensors, the fluctuation of Δn_{air} cannot be measured accurately after restraining the air density noise. The variation of $\delta\Delta n_{\text{air}}$ can be written as

$$\delta\Delta n_{\text{air}} = \delta n_{\text{air},1} - \delta n_{\text{air},2} = n_{\text{air},1}\gamma_1 - n_{\text{air},2}\gamma_2, \quad (11)$$

where γ_1 and γ_2 are the relative refractive index variation coefficients at the position of $(\pi/2)$- and (π)-Raman beams, respectively. In a small enclosed area (about 0.13 m^3), we consider $\gamma_1 = \gamma_2$, Eq. (11) can be simplified as

$$\delta\Delta n_{\text{air}} = \Delta n_{\text{air}}\gamma_1. \quad (12)$$

After using a heat insulation cover, the mean value of Δn_{air} is decreased by an order of magnitude, the value of γ_1 may also decrease because of preventing the air convection, according to Eq. (12), the variation of $\delta\Delta n_{\text{air}}$ is decreased by, at least, one order of magnitude than before. Thus, it can be approximately estimated that the contribution of air density noise to the tilt measurements is below 12 nrad/Hz$^{1/2}$. Besides, the noise of extra Raman laser phase caused by the variation of air length l_{air} is below 2 mrad, and the sensitivity limitation is below 0.5 nrad/Hz$^{1/2}$, far smaller than the current sensitivity of tilt measurements, which can be ignored.

The quantum projection noise (QPN) gives a fundamental limit of the atom interferometer [53], which is related to the total number of atoms that involved in interference. For 1.2×10^4 atoms and the fringe contrast of 28%, the QPN contributes a noise level of 10 nrad/Hz$^{1/2}$ to tilt measurements, which is shown as the black line in Fig. 7.

The detection noise is usually a dominant noise source in atom interferometers by affecting the fluorescence signals, which is related to the detection system. For example, the electronic noise introduced by photodiode dark current and amplifier noise, the laser noise caused by the power or frequency fluctuations of the detection beams [54,55]. The detection noise is evaluated by the method of modulating the number of atoms shown in Ref. [55], and contributing an equivalent noise level of 20 nrad/Hz$^{1/2}$ to tilt measurements.

In addition, the Raman laser phase noise is estimated by the transfer function and the Raman laser phase noise spectroscopy, contributing a noise level of 14 nrad/Hz$^{1/2}$. The tilt noise can be evaluated by a high sampling rate commercial bubble tiltmeter (JEWELL 755) fixed on the mount of the mirror and gives a sensitivity limitation of 6 nrad/Hz$^{1/2}$. As a summary, the sensitivity limitations set by the main noise sources of the tiltmeter are presented in Table I. The total noise is about 39 nrad/Hz$^{1/2}$, which is consistent with the sensitivity of quantum tiltmeter.

V. EARTH TILT TIDES OBSERVATION

Earth tides are a subject that holds a key position in relation to geophysics, geodesy, and astronomy since it is a

TABLE I. Main noise sources to the tilt measurements.

Main noise source	Value (nrad/Hz$^{1/2}$)
Vibration noise	25
Detection noise	20
Raman laser phase noise	14
Air density noise	$\leqslant$12
Tilt noise	6
Quantum projection noise	10
Total	$\leqslant$39

phenomenon that consists of an elastic-viscous deformation of the terrestrial globe, which is caused by the gravitational action of the moon and the sun [25,41]. As one of the Earth tides, Earth tilt tides are quite weak, and the amplitude is only about 10^{-7} rad. It is expected that the Earth tilt tides can be observed by our quantum tiltmeter with the resolution of 1.8 nrad.

In our experiment, the tilt angle β measured by the AI tiltmeter is the angle between the effective wave vector of the Raman beams and the horizontal plane, as well as the angle between the Raman mirror and the plumb line. The tilt of marble platform and Raman mirror will change with the deformation of Earth surface. The Earth tilt tides in the east-west direction can be measured by monitoring the tilt variation of the Raman mirror. A continuous tilt measurement in the east-west direction for 63 h from December 29, 2020 to January 1, 2021 is performed to monitor the Earth tilt tide in the laboratory located in a cave. The black solid line in Fig. 8(a) shows the raw tilt variation of the Raman mirror measured by the quantum tiltmeter, and the violet solid line
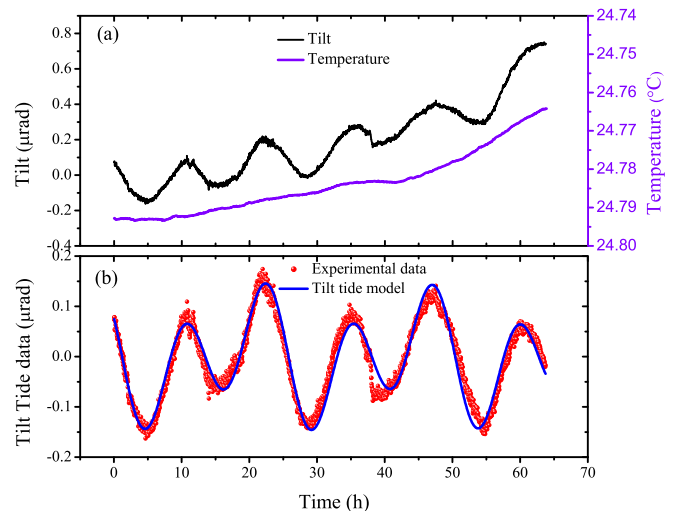

FIG. 8. A continuous tilt measurement in the east-west direction is carried out for 63 h from December 29, 2020 to January 1, 2021. (a) The black line is the tilt variation of Raman mirror measured by the quantum tiltmeter. The purple line is the monitored temperature of room. (b) The red spheres are the experimental tilt tide after correcting the linear drift by temperature. Each data point represents an average of 100 s. The blue line is the theory model of the Earth tilt tide in the east-west direction.

is the room temperature recorded synchronously. Since the thermal expansion effects of the marble platform and mirror mount, the temperature change introduces the drift of tilt. Moreover, we observe that the tilt variation has a delay of 4.5 h compared with the temperature change, possibly due to that the massive marble platform has a long thermal time constant. Through the linear fitting of the tilt and the temperature, we obtain a coefficient of -33.03 nrad/mK. In addition, the sudden tilt change at 38 h is caused by a gathering of people around the laboratory, resulting in a tilt deformation of the ground. After correcting the linear drift of tilt induced by room temperature, the final results of the tilt measurements are the red spheres shown in Fig. 8(b). Each data point represents an average of 100 s. The final experimental data depict the Earth tilt tide with high signal-to-noise ratio and are consistent with the theory model [shown as the blue line in Fig. 8(b)], which shows that this quantum tiltmeter has a great ability in measuring the crustal deformation.

VI. CONCLUSION

In conclusion, we have realized a sensitive quantum tiltmeter with a large scale of MZ-type interferometer. A sensitivity of 40 nrad/Hz$^{1/2}$ for tilt measurements is achieved in our tiltmeter by suppressing the vibration noise and decreasing the effect of air density inhomogeneity. The long-term resolution attains 1.8 nrad within an integration time of 640 s, which is limited by the tilt variation of the retroreflection mirror caused by the fluctuation of room temperature. A continuous Earth tilt tide for 63 h has been observed with high signal-to-noise ratio, which paves the way for measuring the crustal deformation with quantum sensor. In addition, the phase shift of atom interferometer can be written as $\Delta\phi = (k_{\mathrm{eff}}a - \alpha)T^2$, where $a = a_\parallel + g\sin\beta$, $a_\parallel$ is the horizontal acceleration of Raman mirror, which shows that this type of atom interferometer can be used not only as a tiltmeter, but also as a horizontal accelerometer [24,56–59]. According to the Allan deviation of tilt measurements, a sensitivity of 3.9×10^{-7} m/s^2/Hz$^{1/2}$ for horizontal acceleration measurements is obtained. Thus, we can use this type of interferometer to measure tilt angle and horizontal acceleration simultaneously.

[1] A. Peters, K. Y. Chung, and S. Chu, Measurement of gravitational acceleration by dropping atoms, Nature (London) **400**, 849 (1999).

[2] A. Louchet-Chauvet, T. Farah, Q. Bodart, A. Clairon, A. Landragin, S. Merlet, and F. Pereira, Dos Santos, The influence of transverse motion within an atomic gravimeter, New J. Phys. **13**, 065025 (2011).

[3] Z.-K. Hu, B.-L. Sun, X.-C. Duan, M.-K. Zhou, L.-L. Chen, S. Zhan, Q.-Z. Zhang, and J. Luo, Demonstration of an ultrahigh-sensitivity atom-interferometry absolute gravimeter, Phys. Rev. A **88**, 043610 (2013).

[4] S. Abend, M. Gebbe, M. Gersemann, H. Ahlers, H. Müntinga, E. Giese, N. Gaaloul, C. Schubert, C. Lämmerzahl, W. Ertmer, W. P. Schleich, and E. M. Rasel, Atom-Chip Fountain Gravimeter, Phys. Rev. Lett. **117**, 203003 (2016).

[5] J. Fang, J.-G. Lu, X. Chen, H.-R. Zhou, L. Zhou, J.-Q. Zhong, J. Wang, and M.-S. Zhan, Realization of a compact one-seed laser system for atom interferometer-based gravimeters, Opt. Express **26**, 1586 (2018).

[6] X.-J. Wu, Z. Pagel, B. S. Malek, T. H. Nguyen, F. Zi, D. S. Scheirer, and H. Müller, Gravity surveys using a mobile atom interferometer, Sci. Adv. **5**, eaax0800 (2019).

[7] M. J. Snadden, J. M. McGuirk, P. Bouyer, K. G. Haritos, and M. A. Kasevich, Measurement of the Earth's Gravity Gradient with an Atom Interferometer-Based Gravity Gradiometer, Phys. Rev. Lett. **81**, 971 (1998).

[8] N. Yu, J. M. Kohel, J. R. Kellogg, and L. Maleki, Development of an atom-interferometer gravity gradiometer for gravity measurement from space, Appl. Phys. B: Lasers Opt. **84**, 647 (2006).

[9] F. Sorrentino, Q. Bodart, L. Cacciapuoti, Y. H. Lien, M. Prevedelli, G. Rosi, L. Salvi, and G. M. Tino, Sensitivity limits of a Raman atom interferometer as a gravity gradiometer, Phys. Rev. A **89**, 023607 (2014).

[10] X.-C. Duan, M.-K. Zhou, D.-K. Mao, H.-B. Yao, X.-B. Deng, J. Luo, and Z.-K. Hu, Operating an atom-interferometry based gravity gradiometer by the dual-fringe-locking method, Phys. Rev. A **90**, 023617 (2014).

[11] J. B. Fixler, G. T. Foster, J. M. McGuirk, and M. A. Kasevich, Atom Interferometer Measurement of the Newtonian Constant of Gravity, Science **315**, 74 (2007).

[12] G. Rosi, F. Sorrentino, L. Cacciapuoti, M. Prevedelli, and G. M. Tino, Precision measurement of the Newtonian gravitational constant using cold atoms, Nature (London) **510**, 518 (2014).

[13] D. Savoie, M. Altorio, B. Fang, L. A. Sidorenkov, R. Geiger, and A. Landragin, Interleaved atom interferometry for high-sensitivity inertial measurements, Sci. Adv. **4**, eaau7948 (2018).

[14] Z.-W. Yao, H.-H. Chen, S.-B. Lu, R.-B. Li, Z.-X. Lu, X.-L. Chen, G.-H. Yu, M. Jiang, C. Sun, W.-T. Ni, J. Wang, and M.-S. Zhan, Self-alignment of a large-area dual-atom-interferometer gyroscope using parameter-decoupled phase-seeking calibrations, Phys. Rev. A **103**, 023319 (2021).

[15] M. K. Zhou, Z. K. Hu, X. C. Duan, B. L. Sun, J. B. Zhao, and J. Luo, Precisely mapping the magnetic field gradient in vacuum with an atom interferometer, Phys. Rev. A **82**, 061602(R) (2010).

[16] R. Bouchendira, P. Cladé, S. Guellati-Khélifa, F. Nez, and F. Biraben, New Determination of the Fine Structure Constant and Test of the Quantum Electrodynamics, Phys. Rev. Lett. **106**, 080801 (2011).

[17] T. Kovachy, P. Asenbaum, C. Overstreet, C. A. Donnelly, S. M. Dickerson, A. Sugarbaker, J. M. Hogan and M. A. Kasevich, Quantum superposition at the half-metre scale, Nature (London) **528**, 530 (2015).

[18] X.-C. Duan, X.-B. Deng, M.-K. Zhou, K.-Zhang, W.-J. Xu, F. Xiong, Y.-Y. Xu, C.-G. Shao, J. Luo, and Z.-K. Hu, Test of the Universality of Free Fall with Atoms in Different Spin Orientations, Phys. Rev. Lett. **117**, 023001 (2016).

[19] K. Zhang, M.-K. Zhou, Y. Cheng, L.-L. Chen, Q. Luo, W.-J. Xu, L.-S. Cao, X.-C. Duan, and Z.-K. Hu, Testing the universality of free fall by comparing the atoms in different hyperfine states with bragg diffraction, Chin. Phys. Lett. **37**, 043701 (2020).

[20] S. Dimopoulos, P. W. Graham, J. M. Hogan, M. A. Kasevich, and S. Rajendran, Atomic gravitational wave interferometric sensor, Phys. Rev. D **78**, 122002 (2008).

[21] W.-J. Xu, M.-K. Zhou, M.-M. Zhao, K. Zhang, and Z.-K. Hu, Quantum tiltmeter with atom interferometry, Phys. Rev. A **96**, 063606 (2017).

[22] H. Ahlers, H. Müntinga, A. Wenzlawski, M. Krutzik, G. Tackmann, S. Abend, N. Gaaloul, E. Giese, A. Roura, R. Kuhl, C. Lämmerzahl, A. Peters, P. Windpassinger, K. Sengstock, W. P. Schleich, W. Ertmer, and E. M. Rasel, Double Bragg Interferometry, Phys. Rev. Lett. **116**, 173601 (2016).

[23] X.-J. Wu, F. Zi, J. Dudley, R. J. Bilotta, P. Canoza, and H. Müller, Multiaxis atom interferometry with a single-diode laser and a pyramidal magneto-optical trap, Optica **4**, 1545 (2017).

[24] I. Perrin, J. Bernard, Y. Bidel, N. Zahzam, C. Blanchard, A. Bresson, and M. Cadoret, Zero-velocity atom interferometry using a retroreflected frequency-chirped laser, Phys. Rev. A **100**, 053618 (2019).

[25] P. Melchior, *The Tides of the Planet Earth* (Pergamon, Oxford, 1983).

[26] H. Ruotsalainen, Interferometric water level tilt meter development in finland and comparison with combined earth tide and ocean loading models, Pure Appl. Geophys. **175**, 1659 (2018).

[27] J. J. Dvorak and D. Dzurisin, Volcano geodesy: The search for magma reservoirs and the formation of eruptive vents, Rev. Geophys. **35**, 343 (1997).

[28] L. N. Medina, D. F. Arcos, and M. Battaglia, Twenty years (1990-2010) of geodetic monitoring of Galeras volcano (Colombia) from continuous tilt measurements, J. Volcanol. Geotherm. Res. **344**, 232 (2017).

[29] Y. Ito, K. Obara, K. Shiomi, S. Sekine, and H. Hirose, Slow earthquakes coincident with episodic tremors and slow slip events, Science **315**, 503 (2007).

[30] V. Kostoglodov, R. Bilham, J. A. Santiago, V. Manea, M. Manea, and V. R. Hernández, Long-baseline fluid tiltmeter for seismotectonic studies of Mexican subduction zone, Geofis. Int. **41**, 11 (2002).

[31] G. Anderson, S. Constable, H. Staudigel, and F. K. Wyatt, A seafloor long-baseline tiltmeter, J. Geophys. Res.: Solid Earth **102**, 20269 (1997).

[32] W.-J. Xu, L. Cheng, J. Liu, C. Zhang, K. Zhang, Y. Cheng, Z. Gao, L.-S. Cao, X.-C. Duan, M.-K. Zhou, and Z.-K. Hu, Effects of wave-front tilt and air density fluctuations in a sensitive atom interferometry gyroscope, Opt. Express **28**, 12189 (2020).

[33] K. U. Schreiber, T. Klügel, J. P. R. Wells, R. B. Hurst, and A. Gebauer, How to Detect the Chandler and the Annual Wobble of the Earth with a Large Ring Laser Gyroscope, Phys. Rev. Lett. **107**, 173904 (2011).

[34] K. U. Schreiber and J. P. R. Wells, Invited Review Article: Large ring lasers for rotation sensing, Rev. Sci. Instrum. **84**, 041101 (2013).

[35] F. Matichard *et al.*, Seismic isolation of Advanced LIGO: Review of strategy, instrumentation and performance, Classical Quantum Gravity **32**, 185003 (2015).

[36] B. P. Abbott *et al.*, Observation of Gravitational Waves from a Binary Black Hole Merger, Phys. Rev. Lett. **116**, 061102 (2016).

[37] N. F. d'Oreye and W. Züern, Very high resolution long-baseline water-tube tiltmeter to record small signals from Earth free oscillations up to secular tilts, Rev. Sci. Instrum. **76**, 024501 (2005).

[38] F. Boudin, P. Bernard, L. Longuevergne, N. Florsch, C. Larmat, C. Courteille, P. A. Blum, T. Vincent, and M. Kammentaler, A silica long base tiltmeter with high stability and resolution, Rev. Sci. Instrum. **79**, 034502 (2008).

[39] D. C. Agnew, Strainmeters and tiltmeters, Rev. Geophys. **24**, 579 (1986).

[40] Y. Cheng, J. Winterflood, L. Ju, and D. G. Blair, Tilt sensor and servo control system for gravitational wave detection, Classical Quantum Gravity **19**, 1723 (2002).

[41] S. C. Wu, S. H. Fan, J. Luo, and H. Hsu, Folded pendulum tiltmeter, Rev. Sci. Instrum. **73**, 2150 (2002).

[42] A. Takamori *et al.*, Novel compact tiltmeter for ocean bottom and other frontier observations, Meas. Sci. Technol. **22**, 115901 (2011).

[43] J. A. Westphal, M. A. Carr, W. F. Miller, and D. Dzurisin, Expendable bubble tiltmeter for geophysical monitoring, Rev. Sci. Instrum. **54**, 415 (1983).

[44] J. Martínez-Rincón, C. A. Mullarkey, G. I. Viza, W. T. Liu, and J. C. Howell, Ultrasensitive inverse weak-value tilt meter, Opt. Lett. **42**, 2479 (2017).

[45] M. Kasevich and S. Chu, Atomic Interferometry Using Stimulated Raman Transitions, Phys. Rev. Lett. **67**, 181 (1991).

[46] G. Tackmann, P. Berg, C. Schubert, S. Abend, M. Gilowski, W. Ertmer, and E. M. Rasel, Self-alignment of a compact large-area atomic Sagnac interferometer, New J. Phys. **14**, 015002 (2012).

[47] A. Peters, K. Y. Chung, and S. Chu, High-precision gravity measurements using atom interferometry, Metrologia **38**, 25 (2001).

[48] B. Barrett, L. Antoni-Micollier, L. Chichet, B. Battelier, P. A. Gominet, A. Bertoldi, P. Bouyer, and A. Landragin, Correlative methods for dual-species quantum tests of the weak equivalence principle, New J. Phys. **17**, 085010 (2015).

[49] S. Merlet, J. L. Gouët, Q. Bodart, A. Clairon, A. Landragin, F. P. Dos Santos, and P. Rouchon, Operating an atom interferometer beyond its linear range, Metrologia **46**, 87 (2009).

[50] A. Gauguet, T. E. Mehlstäubler, T. Lévèque, J. Le Gouët, W. Chaibi, B. Canuel, A. Clairon, F. Pereira, Dos Santos, and A. Landragin, Off-resonant Raman transition impact in an atom interferometer, Phys. Rev. A **78**, 043615 (2008).

[51] H. Fang, A. Picard, and P. Juncar, A heterodyne refractometer for air index of refraction and air density measurements, Rev. Sci. Instrum. **73**, 1934 (2002).

[52] A. Picard and H. Fang, Three methods of determining the density of moist air during mass comparisons, Metrologia **39**, 31 (2002).

[53] G. Santarelli, P. Laurent, P. Lemonde, A. Clairon, A. G. Mann, S. Chang, A. N. Luiten and C. Salomon, Quantum Projection Noise in an Atomic Fountain: A High Stability Cesium Frequency Standard, Phys. Rev. Lett. **82**, 4619 (1999).

[54] J. Le Gouët, T. E. Mehlstäubler, J. Kim, S. Merlet, A. Clairon, A. Landragin, and F. Pereira, Dos Santos, Limits to the sensitivity of a low noise compact atomic gravimeter, Appl. Phys. B: Lasers Opt. **92**, 133 (2008).

[55] A. Gauguet, B. Canuel, T. Lévèque, W. Chaibi, and A. Landragin, Characterization and limits of a cold-atom Sagnac interferometer, Phys. Rev. A **80**, 063604 (2009).

[56] B. Canuel, F. Leduc, D. Holleville, A. Gauguet, J. Fils, A. Virdis, A. Clairon, N. Dimarcq, C. J. Bordé, and A. Landragin, Six-Axis Inertial Sensor Using Cold-Atom Interferometry, Phys. Rev. Lett. **97**, 010402 (2006).

[57] A. V. Rakholia, H. J. McGuinness, and G. W. Biedermann, Dual-Axis High-Data-Rate Atom Interferometer via Cold Ensemble Exchange, Phys. Rev. Appl. **2**, 054012 (2014).

[58] G. W. Biedermann, X. Wu, L. Deslauriers, S. Roy, C. Mahadeswaraswamy, and M. A. Kasevich, Testing gravity with cold-atom interferometers, Phys. Rev. A **91**, 033629 (2015).

[59] P. Berg, S. Abend, G. Tackmann, C. Schubert, E. Giese, W. P. Schleich, F. A. Narducci, W. Ertmer, and E. M. Rasel, Composite-Light-Pulse Technique for High-Precision Atom Interferometry, Phys. Rev. Lett. **114**, 063002 (2015).